Materials Science & Engineering A 977 (2026) 151108

Contents lists available at ScienceDirect

Materials Science & Engineering A

journal homepage: www.elsevier.com/locate/msea

Evaluation of ductility-dip cracking under elevated-temperature loading in Inconel 738LC fabricated via laser powder bed fusion

Christopher Mercer *, Taisuke T. Sasaki, Yuka Hara, Toru Hara, Masahiro Kusano, Sukeharu Nomoto, Makoto Watanabe

Research Center for Structural Materials, National Institute for Materials Science, Tsukuba, Japan

ARTICLE INFO

Keywords:
Inconel 738LC
Additive manufacturing
Ductility-dip cracking

ABSTRACT

Ductility-dip cracking is a type of solid-state cracking with corresponding ductility loss that is associated with solidification processes in FCC metals and alloys, including Ni-based alloys, at temperatures of typically 0.5 – 0.7 of the alloy melting point. The prevalence of this type of cracking during the tensile deformation of additively manufactured Inconel 738LC at elevated temperature was investigated in this study. Dog bone specimens were machined from IN738LC cylindrical samples fabricated via laser powder bed fusion. Noticeable ductility reduction was observed under tensile loading at 800°C – 900°C. Additionally, it was discovered that extensive cracking at intra-columnar high angle grain boundaries occurred along with significant γ' precipitation, following tensile loading at 900°C. Furthermore, formation of γ' along the high angle intra-columnar grain boundaries was revealed via transmission electron microscopy. The results provide strong evidence for an association between thin, discontinuous grain-boundary γ' precipitation, element segregation and intergranular cracking, consistent with a possible reduction in grain-boundary cohesion and enhanced grain-boundary sliding.

1. Introduction

Inconel 738 is a well-known nickel-based superalloy frequently employed in the hot sections of both land-based and aerospace gas turbine engines [1] on account of its excellent high temperature strength, creep properties and hot corrosion resistance [2,3]. It is a γ' precipitation-strengthened alloy whereby ordered $Ni_3(Al, Ti)$ intragranular precipitates with the $L1_2$ crystal structure provide strengthening by impeding dislocation motion. Like many γ' precipitation-strengthened nickel-based superalloys, IN738 is generally non-weldable due to the relatively high aluminum and titanium content (Al + Ti > 6 wt%) [4]. The high Al + Ti content of this material also affects fabricability via additive manufacturing (AM). The extremely high cooling rates generally associated with 3-D printing processes such as laser powder bed fusion (L-PBF) can lead to cracking during solidification [5–9]. Considerable research has been carried out on the cracking behavior of additively manufactured IN738 and its low-carbon variant IN738LC. Most of the prior work has focused on crack formation during fabrication by various AM techniques. Conclusions are varied, with some researchers reporting solidification cracking due to zirconium segregation [5], whereas others conclude the cracks are, in fact, liquation cracks due to the liquation of low melting point γ + γ' eutectics and/or boride phases along the grain boundaries [6]. Gruber et al. [7] found that both boron and zirconium additions have a strong effect on grain boundary crack formation in L-PBF IN738LC. Boron is a necessary microalloying addition to nickel-based superalloys in general to provide creep resistance but also promotes hot cracking [8]. On the other hand, zirconium may not significantly improve creep resistance but can also promote hot cracking [8]. Other researchers report the presence of both solidification cracks and liquation cracks in AM Inconel 738, again associated with low melting point γ + γ' eutectics [9]. However, most of the prior research agrees that the cracking is intergranular in nature, typically forming along the long columnar grain boundaries in the as-fabricated AM microstructure.

Despite the significant amount of prior work on cracking of IN738 during AM fabrication, little research has been performed on the cracking characteristics of additively manufactured IN738 samples during mechanical loading at elevated temperature. Rickenbacher et al. [10] studied the high temperature material properties of L-PBF fabricated IN738LC and concluded that higher strength can be achieved in the AM material compared to conventionally cast material, but relaxation behavior was found to be inferior.

* Corresponding author.
E-mail address: MERCER.Christopher@nims.go.jp (C. Mercer).

https://doi.org/10.1016/j.msea.2026.151108
Received 24 June 2026; Received in revised form 27 August 2026; Accepted 16 September 2026
Available online 21 September 2026
0921-5093/© 2026 The Authors. Published by Elsevier B.V. This is an open access article under the CC BY license (http://creativecommons.org/licenses/by/4.0/).

Furthermore, a form of solid-state cracking called ductility-dip cracking (DDC) is known to occur during solidification processes such as AM in many Ni-based and other FCC alloys [11–24]. Ductility-dip cracking typically occurs at temperatures of between 0.5 and 0.7 of the melting point of the alloy and, as the term suggests, is associated with a corresponding reduction in ductility. The phenomenon can arise during the solidification process itself or during subsequent re-heating. It has been proposed that DDC is related to grain boundary sliding [14–18] and corresponding strain accumulation. In γ' precipitation-strengthened superalloys, this could be caused by phase-transformation stresses induced in the metal matrix during γ' precipitation [11]. In addition, the formation of grain boundary precipitates may weaken the boundaries [19–22]. Segregation of alloying elements to grain boundaries can also exacerbate this type of cracking [15,16,22–24].

Therefore, a comprehensive, fundamental understanding of all the cracking mechanisms that occur in AM nickel-based superalloys such as IN738, and their effects on mechanical properties, is critical, since it will facilitate the successful prediction and suppression of cracking during AM processing. As part of this effort, the specific purpose of the current study is to investigate the mechanical behavior and cracking mechanisms in IN738LC fabricated via L-PBF when loaded to failure under tension at elevated temperature (600°C – 1000°C). In particular, the effect of DDC on the mechanical properties (especially elongation to failure) is assessed. It should be noted that the materials were purposely deformed in the as-fabricated condition as part of the comprehensive evaluation of cracking/mechanical property relationships in AM nickel-based superalloys. As mentioned above, DDC is a possible mechanism of crack propagation during fabrication, whereby pre-existing defects such as pores and solidification cracks may act as initiation sites, with subsequent propagation as the material passes through the ductility-dip temperature range during the thermal cycling of the AM process. For this reason, an attempt is made to quantitatively investigate the degree of ductility reduction in this temperature range in the as-fabricated condition. Additionally, transmission electron microscopy and atom probe tomography analyses are performed to establish the roles of precipitation and element segregation in the formation of cracks in IN738LC during tensile loading at elevated temperature. Finally, thermodynamic analysis (using the phase-field method) was conducted to determine how the formation mechanisms of γ' in this alloy varied with temperature.

2. Experimental procedure

2.1. Additive manufacturing of Inconel 738LC samples

Spherical Inconel 738LC powder (Höganäs AB, SE-263 83 Höganäs, Sweden) was used in this investigation. The particle size distribution is shown in Fig. 1, and the chemical composition is given in Table 1. Cylindrical specimens were fabricated via laser powder bed fusion (LPBF) using an SLM Solutions SLM280HL laser printer (Nikon SLM Solutions Group AG, Lübeck, Germany). The laser printing parameters employed during the 3-D printing, optimized to mitigate cracking during specimen fabrication, are summarized in Table 2. Scanning pattern rotation angles of 90° and 67° were applied between successive layers as shown in Table 2. The laser beam had a Gaussian profile with a spot size of 80 μm. The printed cylindrical specimens were 75 mm in length and 15 mm in diameter. Dog-bone tensile test specimens were then machined from the cylinders as shown in Fig. 2. Samples of the as-fabricated material were cross-sectioned in XY and XZ orientations (where Z is the build direction) and prepared for metallographic examination using standard polishing procedures.

2.2. Testing and analysis methods

Elevated temperature tensile tests were performed in air under strain control (measured via an extensometer) at a strain rate of 0.3%/min using a mechanical testing device with temperature control (Weld Thermal/Restraint Stress and Strain Cycle Simulator, Fuji electronic

Table 1
Chemical composition of Inconel 738LC powder.

Element	wt%
Nickel	Balance
Aluminum	3.5
Boron	0.007
Carbon	0.1
Cobalt	8.5
Chromium	15.9
Molybdenum	1.7
Niobium	0.88
Tantalum	1.8
Titanium	3.5
Tungsten	2.5
Zirconium	0.024
Oxygen	0.017

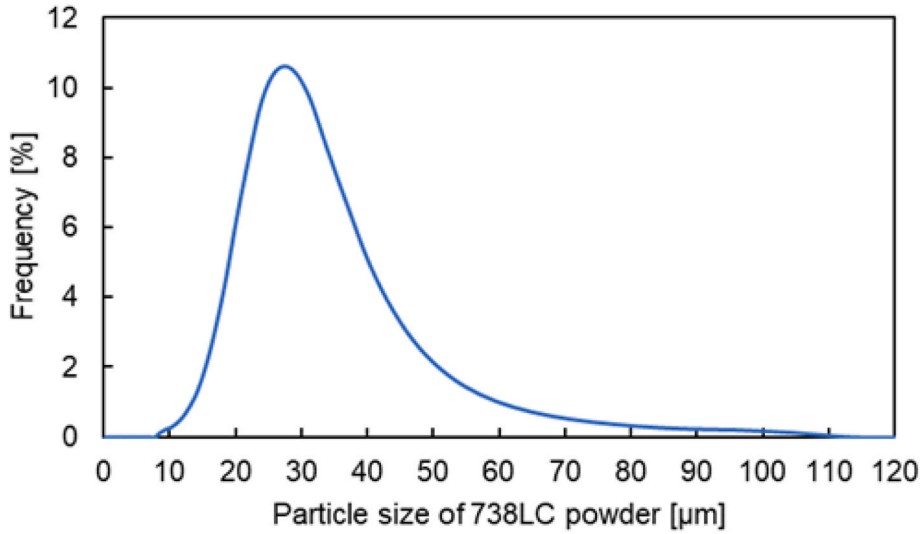


Fig. 1. Particle size distribution of Inconel 738LC powder.

Table 2
Laser printing parameters.

Parameter	Value		
Laser Power (W)	300	300	300
Laser Scanning Speed (mm/s)	1100	1500	1500
Hatch Spacing (μm)	100	100	100
Slice Thickness (μm)	30	30	30
Laser Rotation Angle	90°	90°	67°
Identification Code	LS1100-RA90	LS1500-RA90	LS1500-RA67

Industrial Co. Ltd., Japan). As stated in the introduction, the specimens were tested in the as-fabricated condition to allow a meaningful comparison with cracking phenomena typically observed during L-PBF processing. The samples were heated by electrical resistance heating and the heating rate was controlled so that the test temperature was reached within 10 s. Tests were conducted at 600°C, 700°C, 800°C, 900°C and 1000°C until fracture occurred. Up to three tensile specimens were tested for each condition, depending on specimen availability. In accordance with standard tensile testing practice, specimens that fractured outside the gauge section (e.g. within the grips) were regarded as invalid and were not included in the analysis. The results presented are therefore based on valid tensile tests.

Following tensile testing at 600°C and 900°C, the fractured tensile specimens fabricated at a scanning speed of 1100 mm/s and a scan rotation angle of 90°, (LS1100-RA90), were sectioned along their longitudinal axis such that the sectioning plane passed through the fracture surface. The sections were then also prepared for metallographic examination to allow comparison with the undeformed material. Although a scan rotation of 67° often results in fewer defects, material fabricated using a scan rotation angle of 90° was purposely studied for two reasons: (i) prior optimization of AM process parameters ensured that little discernible cracking was present in the as-built material using a scan speed of 1100 mm/s and scan rotation angle of 90°; and (ii) the emergence of cracks during tensile deformation is more easily identified and observed in the straight, columnar microstructure characteristic of a 90° scan rotation angle.

The polished surfaces and fractures surfaces were examined via light microscopy (VHX-2000, Keyence Corporation, Osaka, Japan) and scanning electron microscopy (SEM); Auriga-Laser, Carl Zeiss Microscopy GmbH (ZEISS), Jena, Germany. Electron backscatter diffraction (EBSD) analysis equipped on the SEM was also performed to determine grain orientation and to identify high-angle grain boundaries. Images were analyzed using ImageJ software (National Institutes of Health, Bethesda, MD, USA) to measure average crack length and total crack length per unit area (crack density). A minimum crack length threshold of 20 μm was applied to ensure consistent identification and to exclude very small crack-like features.

Following the SEM and EBSD characterization, a focused ion beam–scanning electron microscope (FIB–SEM); Scios 2, Thermo Fisher Scientific, Waltham, MA, USA) was employed to fabricate specimens for transmission electron microscopy (TEM) analysis. The TEM specimens were taken across high-angle grain boundaries identified by the EBSD analysis in order to assess grain boundary segregation during fabrication and elevated temperature tensile testing. The TEM analysis was performed using a JEM-2800 (JEOL, Tokyo, Japan) in bright-field TEM and STEM modes. Energy-dispersive spectroscopy (EDS) was utilized to generate element maps from regions of interest in the samples.

Finally, needle specimens for atom probe tomography (APT) were fabricated from high angle grain boundary regions of the specimens tested at 600°C and 900°C, using a Thermo Scientific Helios G4 focused-ion beam SEM (Thermo Fisher Scientific, Waltham, Massachusetts, U.S.A.). The APT analysis was then performed using a CAMECA LEAP5000XS in laser-pulsing mode, in order to study elemental segregation at the grain boundaries. The specimen temperature, detection rate, pulse energy and pulse rate were 50K, 0.5, 50 pJ and 250 kHz, respectively. Data reconstruction was carried out using CAMECA IVAS 3.8.0 software.

3. Results

3.1. Analysis of initial (as-fabricated) microstructures and cracking

Microstructures of the as-fabricated material, prior to tensile deformation, are presented in Fig. 3. At a scan rotation angle of 90°, the structure exhibits straight, columnar grains arranged in a grid pattern on the XY plane. The pattern is a little less uniform at the faster scanning speed of 1500 mm/s. At 67°, the grains exhibit a more irregular structure. Very little porosity and cracking was observed in the material fabricated at a scanning speed of 1100 mm/s, due to process optimization. Quantitative image analysis determined an average crack length of 42 ± 25 μm (mean ± standard deviation), and a mean crack density of 0.07 mm^{-1}.

3.2. Tensile tests

The tensile stress-strain curves for the samples fabricated using a laser scanning speed of 1100 mm/s and a scanning pattern rotation angle of 90°, for each test temperature are presented in Fig. 4 (a). The maximum stress is significantly less at 900°C compared to the other testing temperatures. Tensile strength and elongation to failure as a function of testing temperature are

shown in Fig. 4(b) and (c), respectively. A decreasing trend of tensile strength with increasing test temperature is evident in Fig. 4 (b). A marked reduction in ductility is evident at 700°C which reaches a minimum at temperatures between 800°C and 900°C (Fig. 4 (c)). Ductility was shown to increase again at temperatures beyond 900°C. Typical data for conventionally cast and heat treated Inconel 738 [25] is also shown in Fig. 4 (c) for comparison, i.e. to show an ideal target level of ductility. No ductility dip is observed in the cast material.

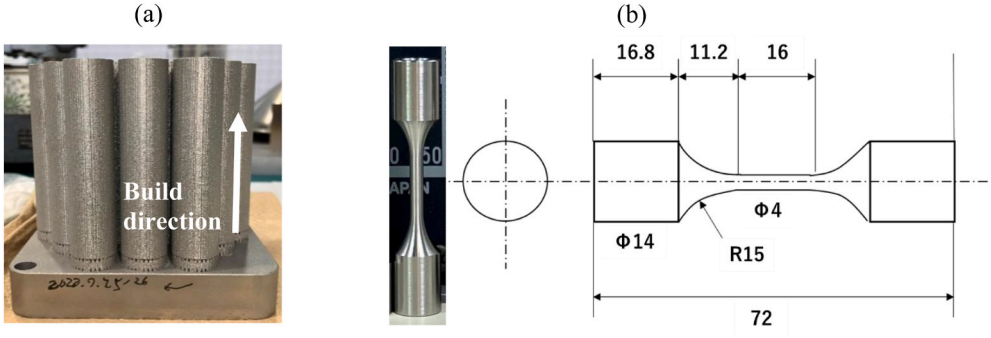


Fig. 2. (a) Laser printed Inconel 738LC cylinders, (b) Dog-bone tensile test specimens (dimensions are in mm).

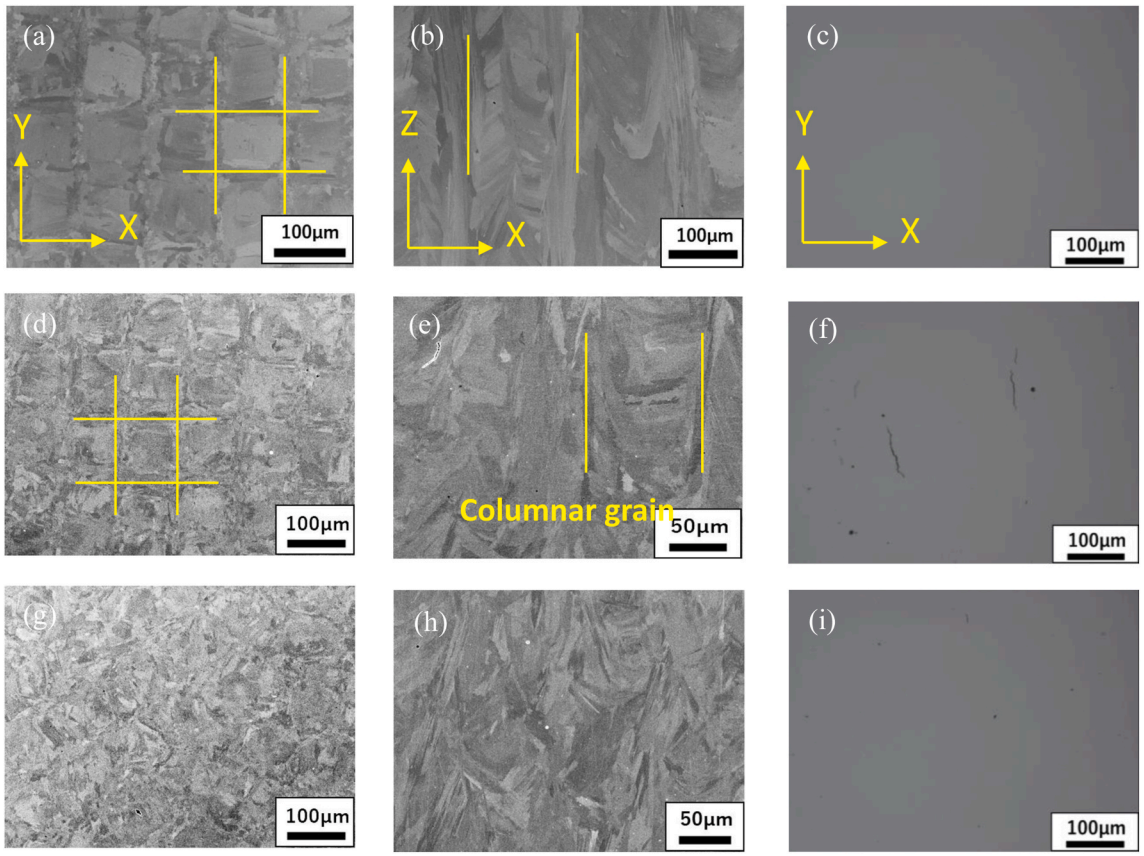


Fig. 3. Scanning electron and light micrographs showing microstructure and cracking in the as-built IN738LC material for different scanning speeds and scan rotation angles. (a)-(c) LS1100-RA90; (d-f) LS1500-RA90; and (g-i) LS1500-RA67. (Images (a), (d) and (g) and (b), (e) and (h), left and center columns respectively, are SEM micrographs (2 kV, ETD). Images (c), (f) and (i) (right column) are light micrographs).

3.3. *Analysis of fractured samples*

The fracture surfaces of the specimen fabricated at a scanning speed of 1500 mm/s are shown in Figs. 5 and 6 for a scan rotation angle of 90° and 67°, respectively. At 600°C, a typical ductile-dimple-like fracture surface was observed (Fig. 5 (a)). However, at 900°C, the fracture surface exhibited a square grid or "lattice-like" appearance (Fig. 5 (b)), similar to the as-fabricated microstructure. The material fabricated using a rotation angle of 67° also exhibited ductile dimple fracture at the lower testing temperatures but a more irregular "lattice-like" morphology at higher temperatures (Fig. 6).

Polished cross-sections taken through the fracture surfaces of specimens fabricated at a scanning speed of 1100 mm/s and a scan rotation of 90° (LS1100-RA90) and tested at 600°C and 900°C, are shown in Figs. 7 and 8, respectively. The microstructure of the samples consisted of straight, columnar grains aligned with the build direction. The fracture surface following tensile loading to failure at 600°C is inclined at an angle of approximately 45° to the loading axis (Fig. 7 (a)). No cracks or γ' precipitates were visible via SEM at this testing temperature. The fracture surface following testing at 900°C, however, is perpendicular to the loading axis and has a serrated appearance (Fig. 8 (a)). Moreover, extensive intra-columnar grain cracking is observed in the vicinity of the fracture surface (Fig. 8 (a)) and significant γ' precipitation is evident (Fig. 8 (c)). A total of 65 cracks were identified in the region near the fracture surface. The average crack length was 65 μm with a standard deviation of 29 μm. The corresponding crack-length density was 1.16 mm^{-1}. The cracks exhibited an asymmetric V-shaped morphology, and the orientations of both crack arms were measured for a representative subset of 25 cracks distributed across the analyzed region. The crack arms were oriented at 47 ± 13° relative to the build direction, with a mean included angle of 113 ± 24°.

An inverse pole figure (IPF) map produced by EBSD from the region exhibiting cracking in the specimen tested at 900°C (specifically the area shown in Fig. 8 (b)) is presented in Fig. 9(a).

The IPF shows that the cracks occur at high angle grain boundaries between successive layers of the additively manufactured structure. The cracks were confined to the vertical columnar grains and did not extend into neighboring columns. Approximately 50% of the cracks coincided with high angle grain boundaries. The corresponding KAM map (Fig. 9 (b)) reveals pronounced misorientation along the columnar grain boundaries, most notably in the regions adjacent to the crack tips.

Fig. 10 shows an IPF and corresponding KAM map for a selected region of intergranular cracking. The IPF shows that the crack follows several grain boundaries. Most of the cracking occurs along a high angle boundary. The KAM map clearly shows a region of localized high KAM at the tip of the crack that indicates localized plastic deformation associated with crack propagation.

Fig. 11 is an electron micrograph of the specimen tested at 900°C showing the location (marked using carbon deposition) at which focus ion beam cutting was performed to extract a thin sample of material suitable for TEM observation. The location was chosen so that the TEM specimen includes the indicated high angle grain boundaries that are located near to one of the intra-columnar cracks. The rationale behind this was to identify any grain boundary segregation that could be responsible for the observed cracking. Specimens were also extracted from similar high angle grain boundaries in the sample tested at 600°C for comparison purposes.

Scanning-transmission electron microscopy (STEM) images and corresponding EDS element maps from regions exhibiting high angle grain boundaries are shown in Figs. 12 and 13, for the specimens tested

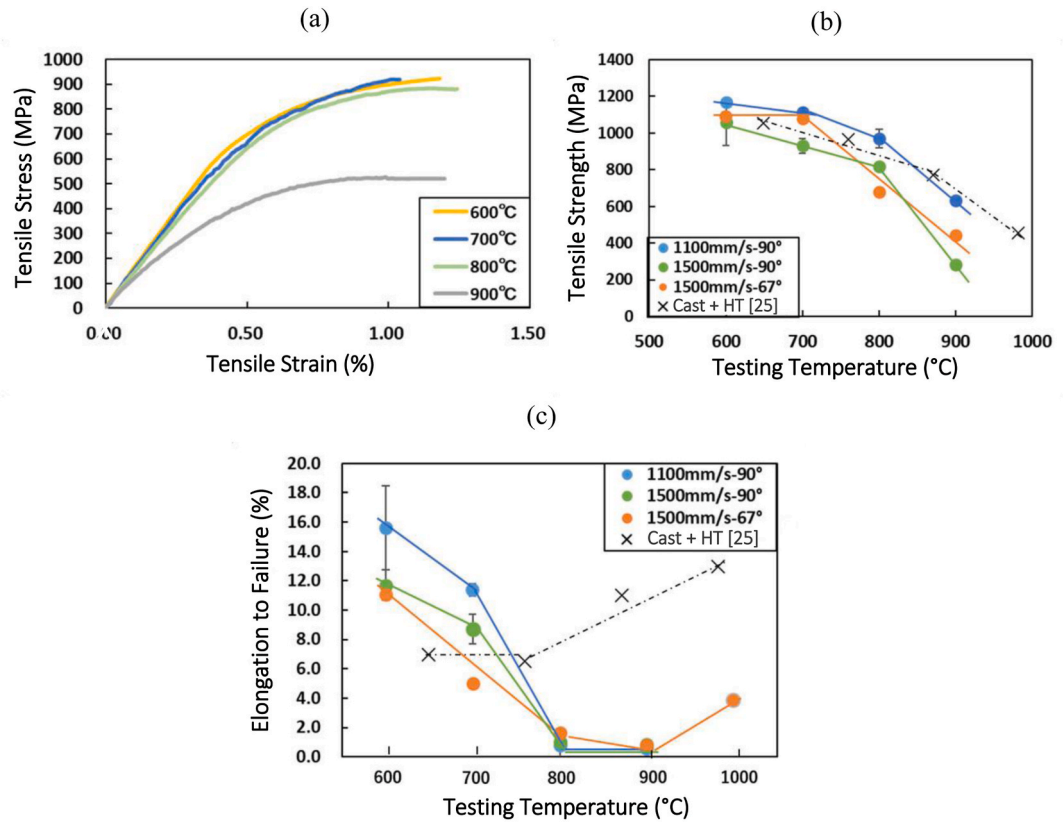


Fig. 4. (a) Tensile stress-strain curves for LS1100-RA90 at various testing temperatures; (b) tensile strength as a function of temperature; and (c) elongation to failure as a function of temperature, for different printing conditions. The values presented with error bars represent the mean ± standard deviation of the valid tests. Where no error bar is visible, either only a single valid result was available, or the standard deviation is smaller than the data-point marker.

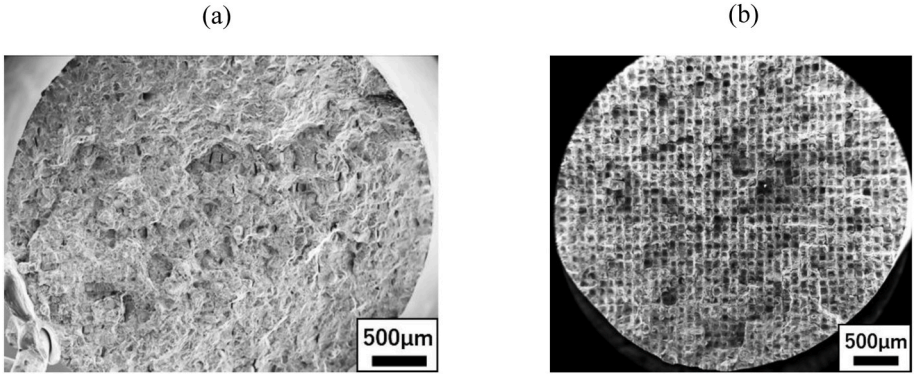


Fig. 5. Fracture surfaces of LS1500-RA90 following testing under tensile loading at (a) 600°C and (b) 900°C. (5 kV, ETD.)

at 600°C and 900°C, respectively.

It can be seen from Fig. 12 that there is a slight concentration of titanium at the high angle grain boundary and a corresponding slight depletion of nickel. Maps of other selected elements show a uniform distribution. However, maps of a high angle grain boundary region in the sample tested at 900°C clearly show a strong concentration of nickel, aluminum and titanium at the boundary. A corresponding depletion of other elements, such as chromium and cobalt, is also markedly evident (Fig. 13). No oxygen was detectable by EDS in the grain boundary regions of either material. The TEM observation also revealed a cell structure within the grains. It is surmised that the cell walls are comprised of dislocation tangles. A STEM image and corresponding elements maps of the cell structure are presented in Fig. 14. A similar phenomenon was observed; i.e. a concentration of nickel, aluminum and titanium at the cell walls and a corresponding depletion of other elements.

3D atom probe analyses were conducted in the vicinity of cracks located at high-angle grain boundaries. Fig. 15 (a) presents a 3D atom map of Ni, Cr, B, and C obtained from the fractured sample at 600°C with a reconstructed volume of 41 × 41 × 193 nm^3. A 1-nm-thick slice of the reconstructed volume is shown together with 16.5 at.% Cr iso-concentration surfaces to highlight nanoscale elemental fluctuations that could not be resolved by STEM-EDS elemental mapping in Fig. 12. A proximity diagram (proxigram) analyzed across the Cr iso-concentration surface reveals that the Cr-rich regions are also enriched in the γ-former element of Co, whereas γ′-forming elements such as Ni, Al, and Ti are

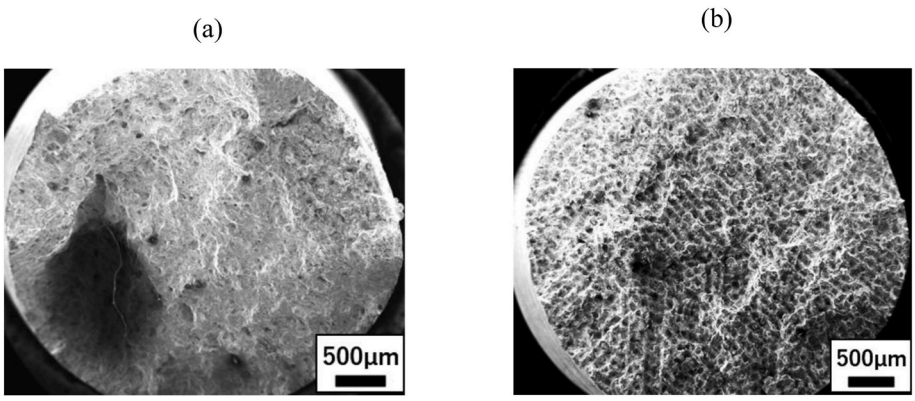


Fig. 6. Fracture surfaces of LS1500-RA67 following testing under tensile loading at (a) 600°C and (b) 900°C. (5 kV, ETD.)

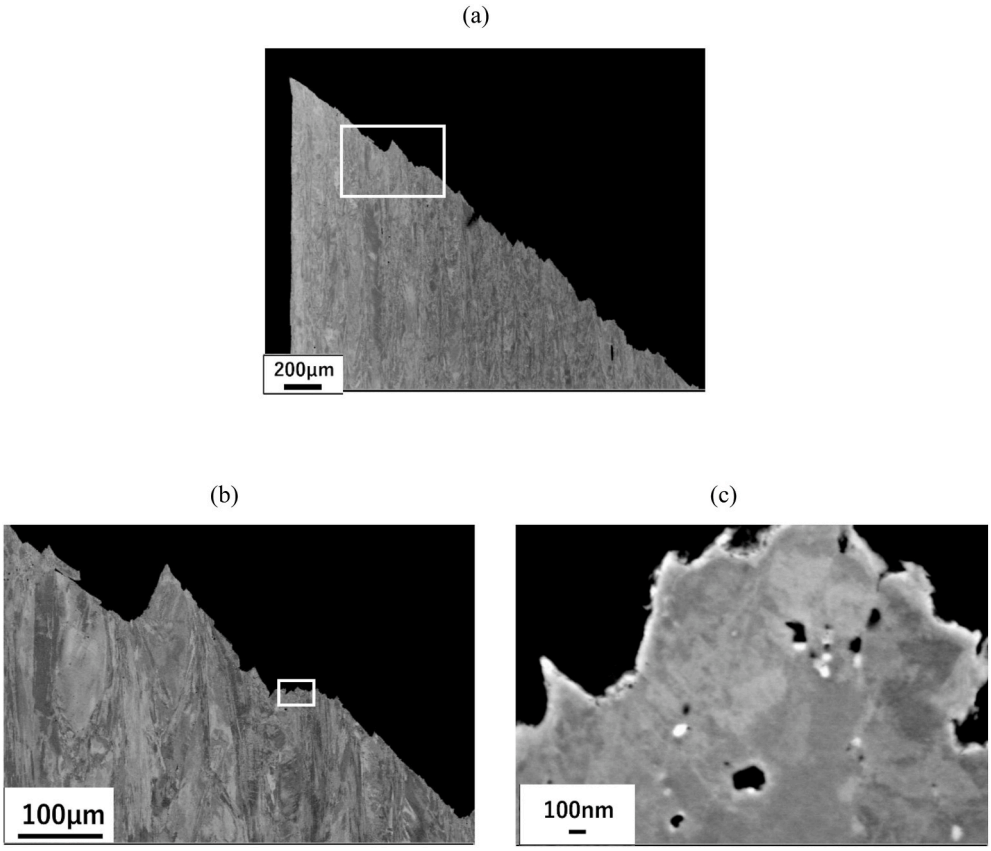


Fig. 7. Scanning electron micrographs of the polished cross-section of LS1100-RA90 following testing at 600°C. (a) Low magnification image of fracture surface (5 kV, retractable BSD, Auriga); (b) Detail of highlighted region in (a) (5 kV, retractable BSD, Auriga); and (c) detail of highlighted region in (b) (5 kV, retractable BSD, Auriga).

preferentially partitioned into the Cr-lean/Ni-rich regions, as shown in Fig. 15 (b). The chemical compositions of the Cr-rich and Cr-lean regions are $Ni_{48.1}Cr_{28.3}Co_{12.4}Al_{4.6}Ti_{3.0}W_{0.7}$- $Ta_{0.3}Mo_{1.9}Nb_{0.3}C_{0.1}B_{0.3}$ and $Ni_{61.0}Cr_{7.3}Co_{10.1}Al_{8.8}Ti_{8.1}W_{0.7}Ta_{0.6}Mo_{1.7}Nb_{0.4}C_{0.4}B_{0.3}$ in at.%, respectively. Furthermore, the Ni-rich region exhibits an interconnected morphology rather than isolated particles. These features indicate that the tensile deformation at 600°C promotes a spinodal-like decomposition of γ′ precipitates from the γ matrix, consistent with recent reports [26].

The enrichment of B in Fig. 15 (a) enables the identification of a grain boundary, as indicated by an arrow. The B distribution demonstrates pronounced heterogeneity in elemental segregation along the grain boundary. As shown in the 1D compositional profile across the Cr-rich grain boundary in Fig. 15(c)–B, C, and Mo exhibit clear enrichment at the grain boundary. The corresponding contents of B, C, and Mo are 1.5, 0.5, and 2.9 at.%, respectively. In contrast, only minor elemental segregation is observed at the grain boundaries at the Cr-lean region, as evidenced by the 1D compositional profile in Fig. 15 (d).

Tensile testing at 900°C results in the formation of a significantly coarser γ-γ′ two-phase microstructure compared with that observed after the deformation at 600°C, as illustrated by the 3D atom map in Fig. 16 (a). Fig. 16 (b) shows a 1D compositional profile across a γ-γ′ phase boundary, indicating that the γ and γ′ phase have a chemical composition of $Ni_{48.8}Cr_{31.2}Co_{14.4}Al_{0.9}$-$Ti_{0.9}W_{1.0}Ta_{0.6}Mo_{2.1}Nb_{0.2}Zr_{0.03}B_{0.02}$ and $Ni_{67.1}Cr_{11.1}Co_{5.7}Al_{3.7}Ti_{8.3}W_{1.0}Ta_{1.2}Mo_{0.9}Nb_{1.0}Zr_{0.04}B_{0.02}$ in at.%, respectively. Notably, the grain boundary indicated by an arrow in

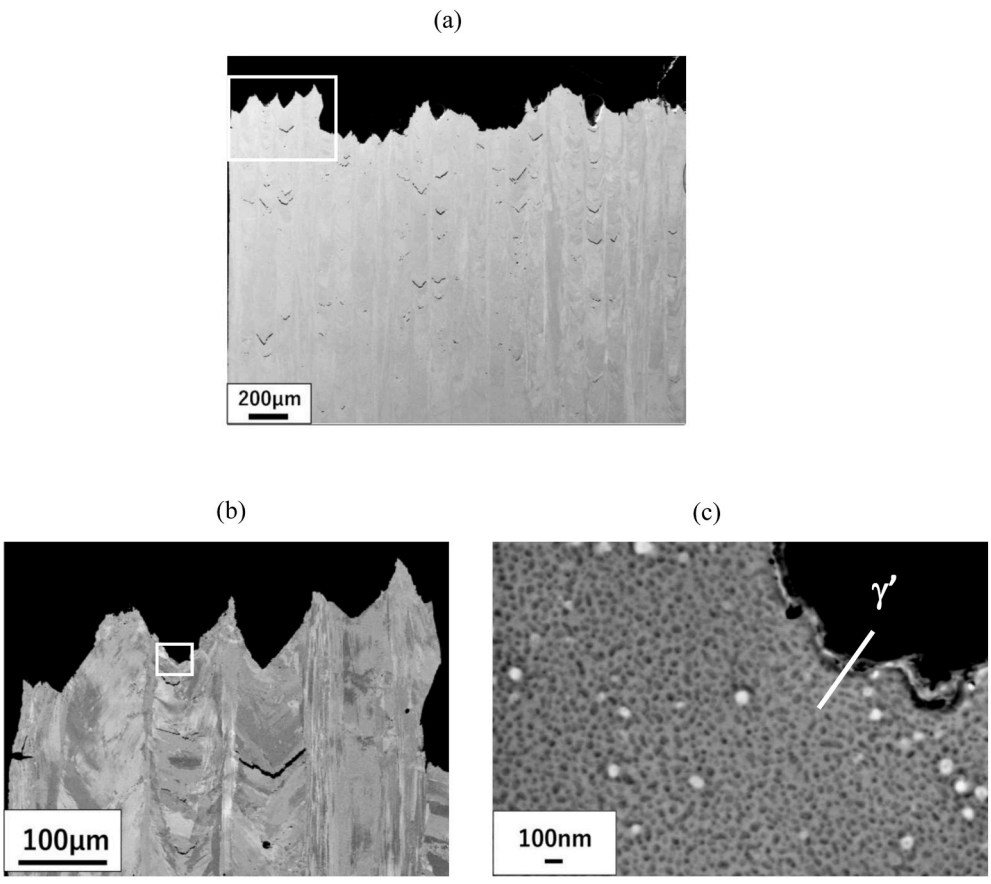


Fig. 8. Scanning electron micrographs of the polished cross-section of LS1100-RA90 following testing at 900°C. (a) Low magnification image of fracture surface (5 kV, ETD); (b) Detail of highlighted region in (a) (5 kV, retractable BSD, Auriga); and (c) detail of highlighted region in (b) (5 kV, retractable BSD, Auriga).

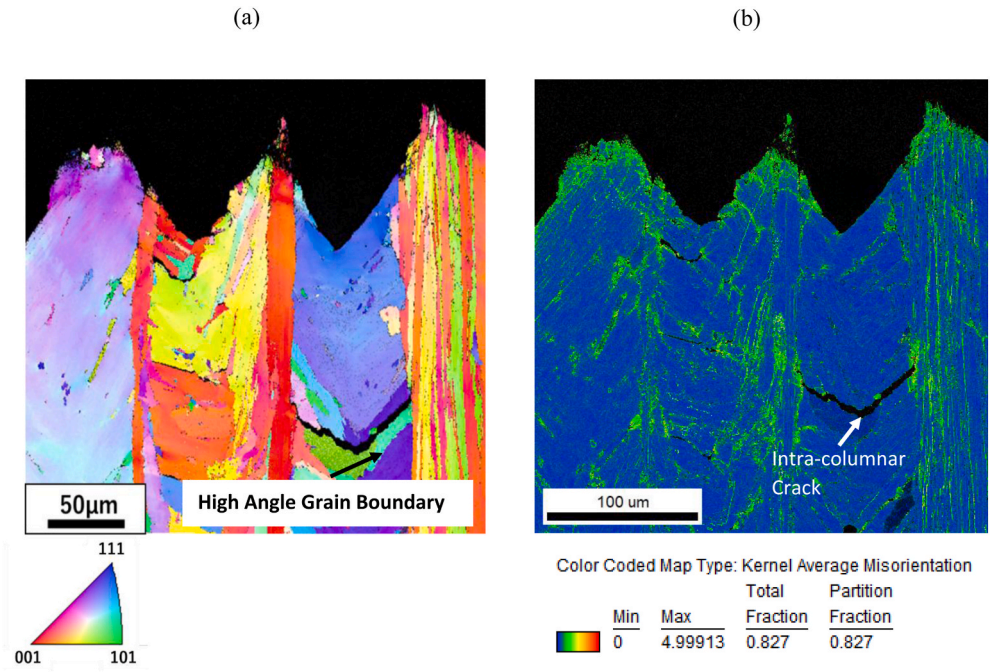


Fig. 9. (a) An EBSD inverse pole figure (IPF) map; and (b) a KAM map, of the polished cross-section of LS1100-RA90 following testing at 900°C. The same region as that shown in Fig. 8(b). (20 kV, 0.3 μm step).

Fig. 16 (a) separates γ-γ, γ-γ′, and γ′-γ′ phase regions. Fig. 16 (c) presents a 1D compositional profile across the grain boundary separating the two neighboring γ′ precipitates. At the γ′-γ′ boundary, slight enrichment of γ-forming elements such as Cr and Co is observed, while the segregation

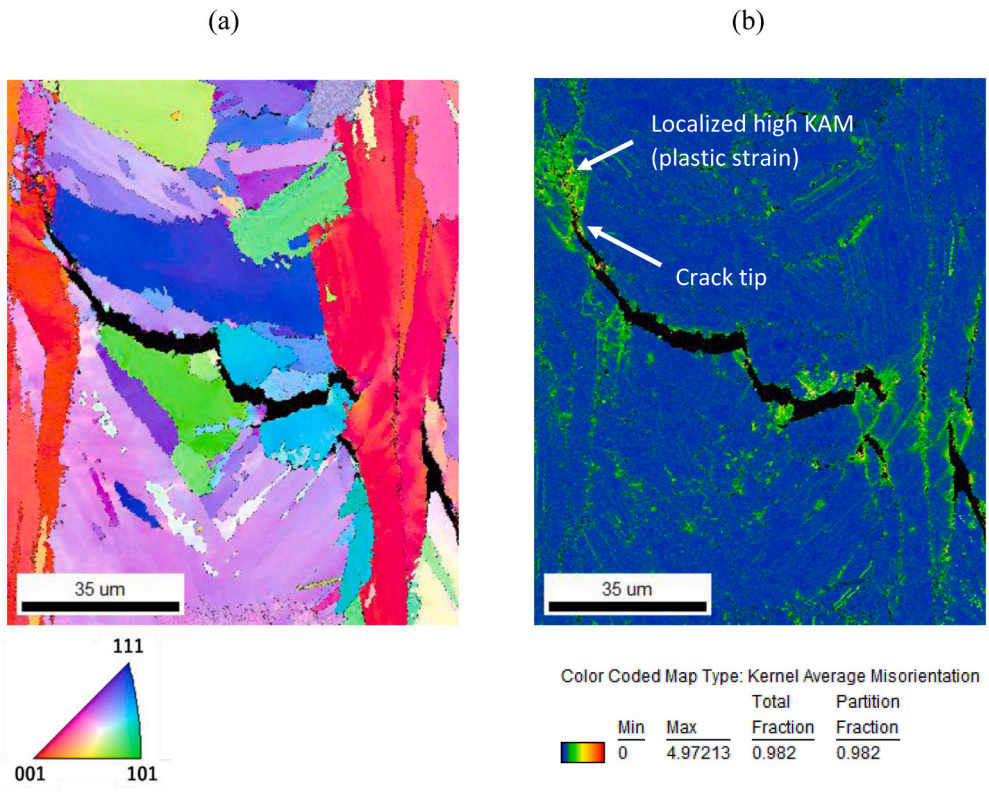


Fig. 10. (a) An EBSD inverse pole figure (IPF); and (b) a KAM map, of the polished cross-section of LS1100-RA90 following testing at 900°C showing detail of intergranular cracking. (20 kV, 0.2 μm step).

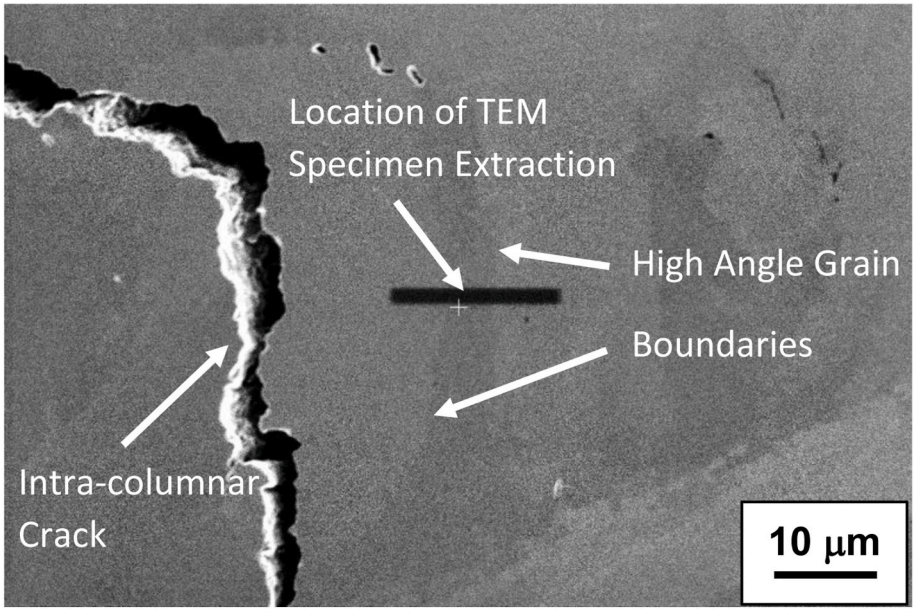


Fig. 11. Scanning electron micrograph showing position of TEM specimen extracted via FIB cutting from the polished cross-section of LS1100-RA90 following testing at 900°C (5 kV, ETD).

of B, C, Mo is the weakest among these three boundaries. The corresponding contents of B, C, and Mo are 0.2, 0.04, and 1.3 at.%, respectively. Elemental segregation at the grain boundary separating γ-γ and γ-γ′ phase regions are further analyzed by extracting the selected volume shown in Fig. 16 (d). At the γ-γ boundary, B, C, and Mo exhibit pronounced segregation, accompanied by slight depletion of Ni, as shown in the 1D compositional profile in Fig. 16 (e). The contents of B, C, and Mo at this boundary are 1.1, 0.3, and 2.7 at.%, respectively. Similar segregation behavior of B, C, Mo is observed at the γ-γ′ boundary, with concentrations of 0.7, 0.1, 2.5 at.%, respectively, as shown in Fig. 16 (f). It should be noted that no significant grain boundary oxygen concentration was detected via APT at either testing temperature. In fact, oxygen levels are negligibly low. Therefore, it can be concluded that oxidation does not play a role in the observed DDC behavior.

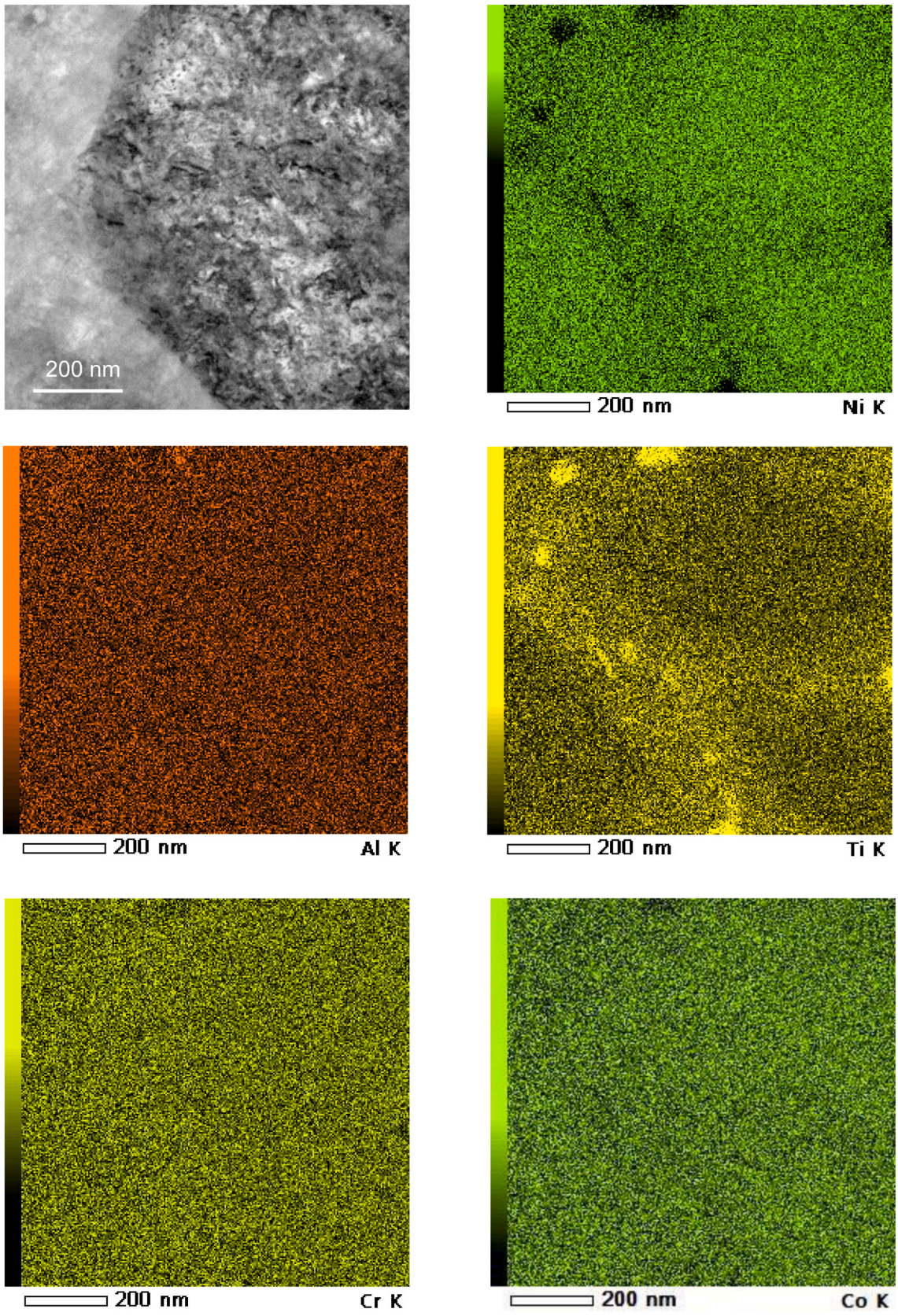


Fig. 12. Scanning-transmission electron microscopy (STEM) image and EDS element maps from a high angle grain boundary region of the LS1100-RA90 specimen tested at 600°C.

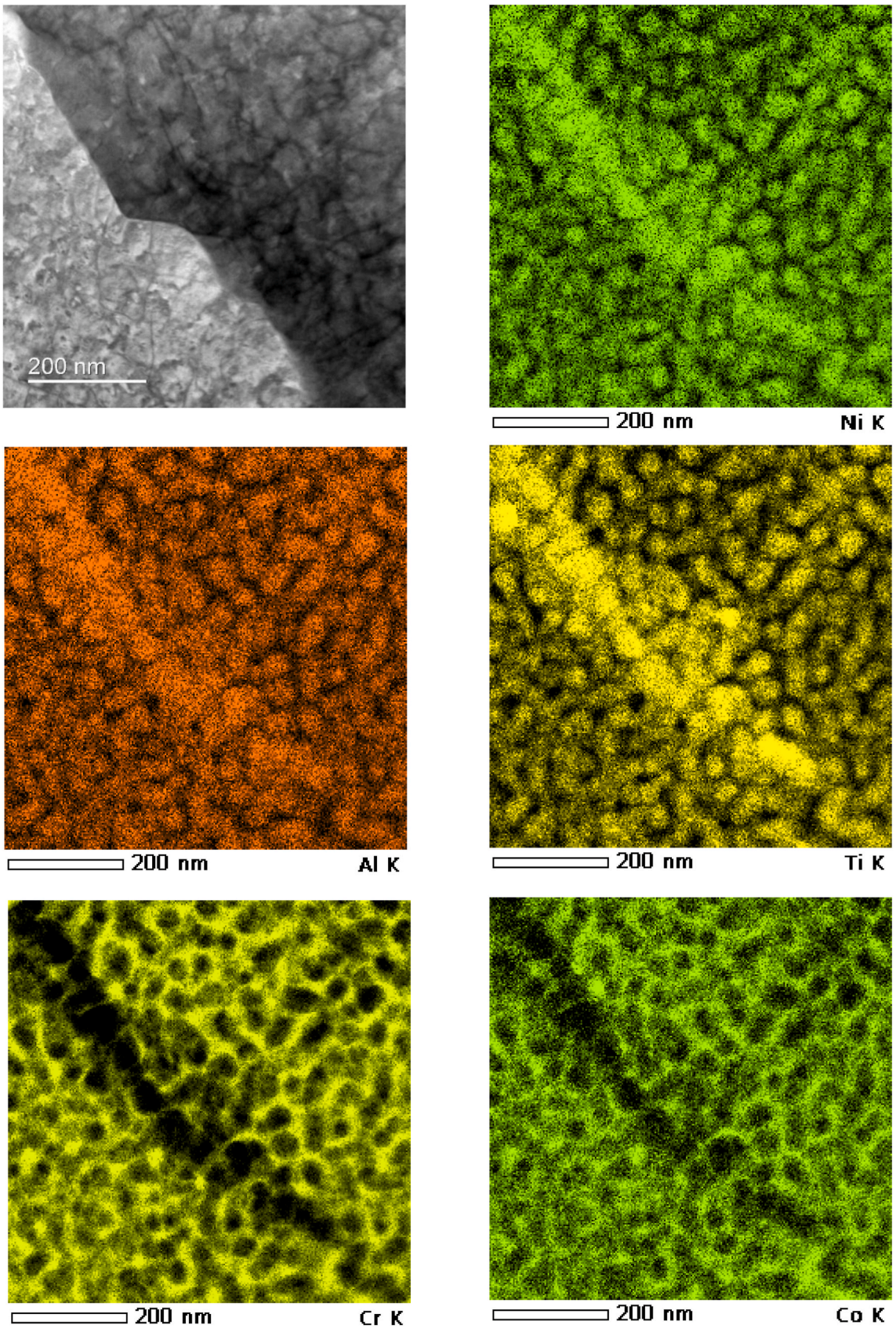


Fig. 13. Scanning-transmission electron microscopy (STEM) image and EDS element maps from a high angle grain boundary region of the LS1100-RA90 specimen tested at 900°C.

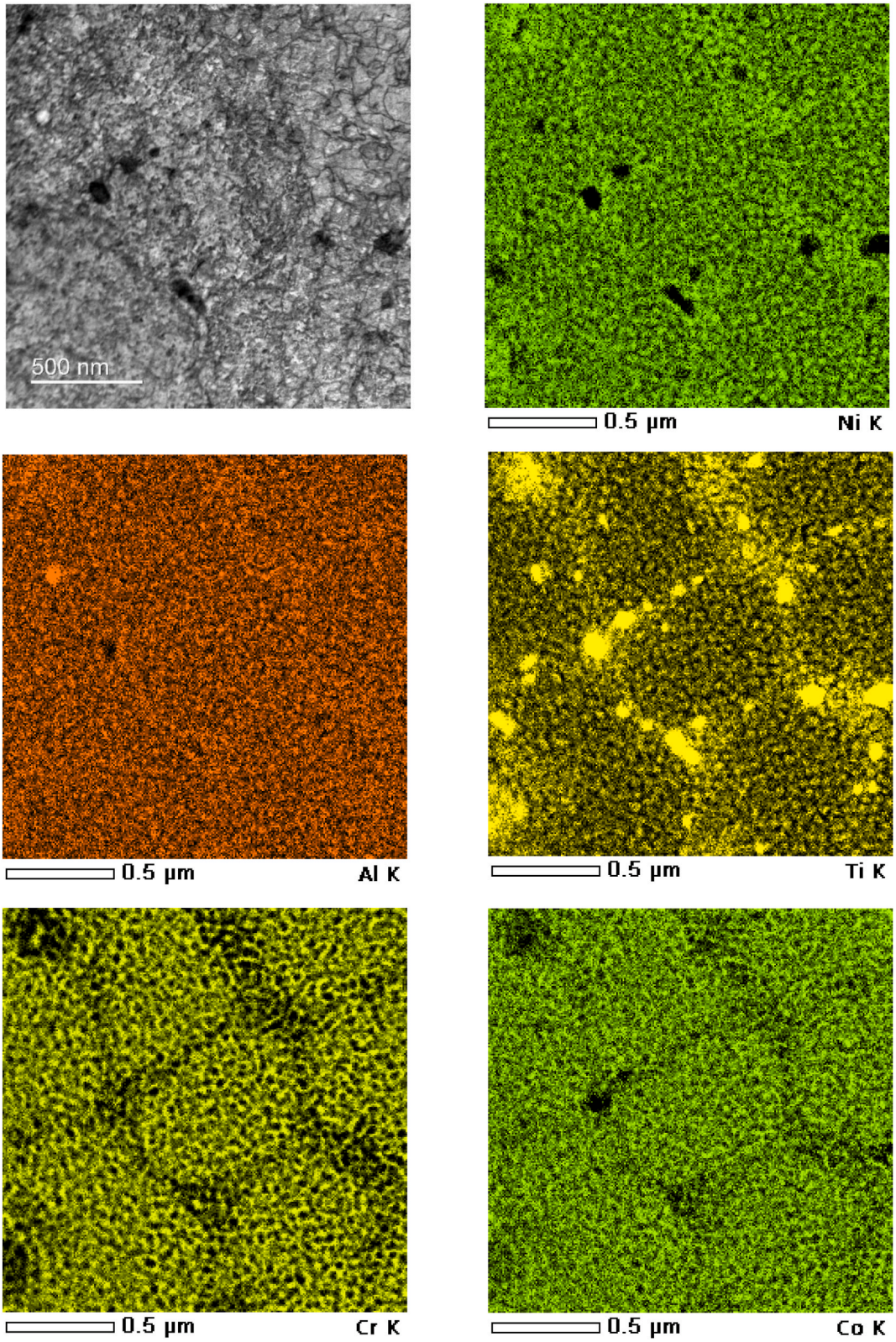


Fig. 14. Scanning-transmission electron microscopy (STEM) image and EDS element maps of cell structure in the specimen LS1100-RA90 tested at 900°C.

It is important to note that although multiple processing conditions were investigated to evaluate mechanical behavior, the mechanistic interpretation presented here is based primarily on the detailed characterization of the 1100 mm/s, 90° specimens. The additional processing conditions provide supporting evidence for the generality of the observed mechanical response but are not intended to imply that the cracking behavior is identical for all processing conditions.

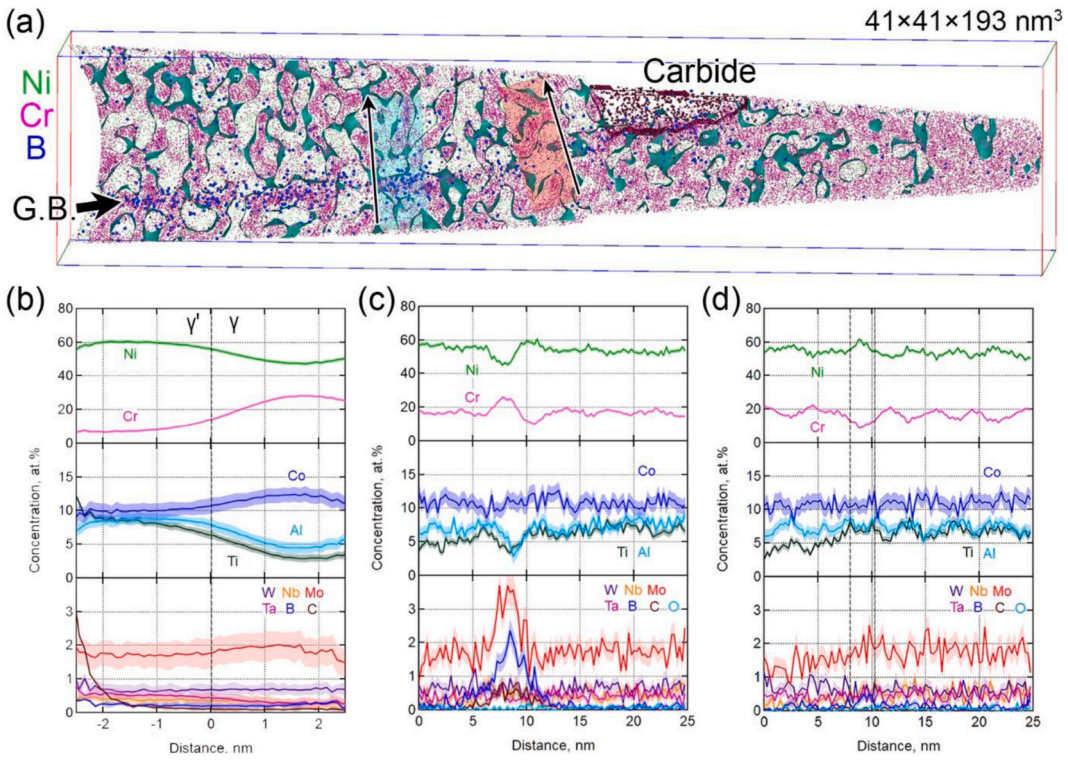


Fig. 15. (a) 3D atom map of the fractured specimen LS1100-RA90 after tensile testing at 600°C. (b) Proximity diagram (proxigram) across the iso-concentration surface of 16.5 at.% Cr. (c) and (d) are 1D compositional profile obtained from a selected volume with 10 × 10 × 25 nm^3 with light blue and pink color, respectively. (For interpretation of the references to color in this figure legend, the reader is referred to the Web version of this article.)

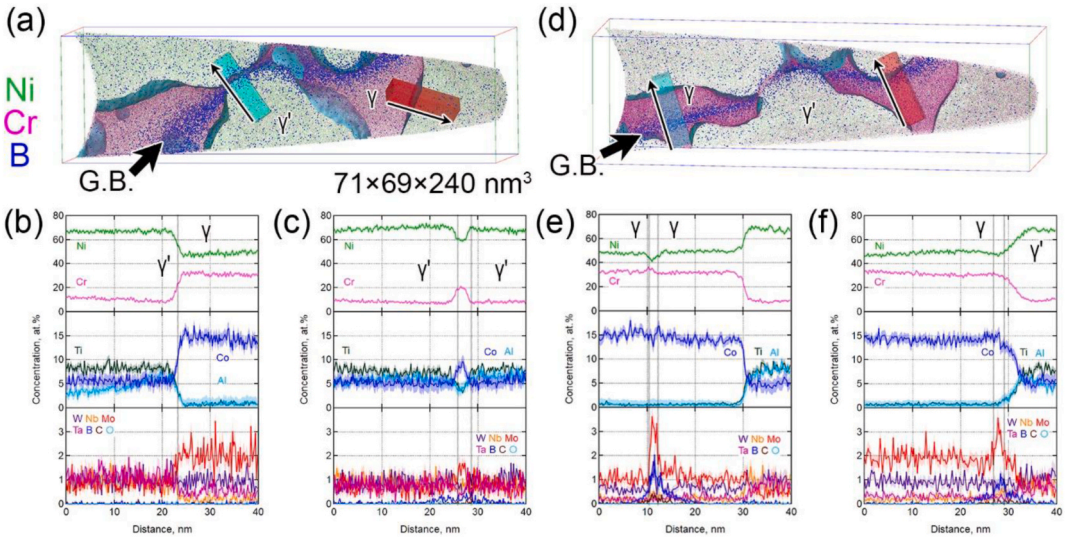


Fig. 16. (a) 3D atom map of the fractured specimen LS1100-RA90 after tensile testing at 900°C. (b) and (c) are 1D compositional profile obtained from a selected volume with 10 × 10 × 40 nm^3 with red and light blue color, respectively. (d) 3D atom map viewing from a different angle of (a). (e) and (f) are 1D compositional profile obtained from a selected volume with 10 × 10 × 40 nm^3. Note that the grain boundary in (e) and (f) separates the γ-γ and γ-γ′ phase regions, respectively. (For interpretation of the references to color in this figure legend, the reader is referred to the Web version of this article.)

4. Discussion

The tensile tests revealed a marked reduction in ductility between 800°C and 900°C. Microscopy analysis of the fracture surface region revealed many intra-columnar cracks in the vicinity of the fracture surface. Significant γ' precipitation was also observed at 900°C. The presence of the cracks and associated ductility reduction is a clear indication of ductility-dip cracking (DDC). Furthermore, a concentration of nickel, aluminum and titanium was observed at high angle intra-columnar grain boundaries following testing at 900°C. These are the three elements that comprise the γ' phase. Therefore, it appears that γ' is formed along the high angle intracolumnar grain boundaries in a thin discontinuous layer via the segregation of Ni, Al and Ti at 900°C. The intermittent γ' layer has an average thickness of 42 nm, a continuity of approximately 90% and co-exists with the FCC γ phase, maybe as part of a γ/γ' eutectic-type microstructure.

Although cracking in IN738 during additive manufacturing is often attributed to solidification cracking, liquation cracking, or the presence of low-melting γ/γ' eutectics, these mechanisms require localized melting and resolidification. In the present work, tensile testing was conducted at temperatures well below the alloy solidus, where any cracking occurs entirely in the solid state. Furthermore, no evidence of resolidified eutectic structures, grain-boundary rounding, or other features indicative of grain-boundary melting were observed in the as-built microstructures. The observed intergranular cracking is therefore consistent with a solid-state mechanism associated with grain-boundary γ' film formation and elemental segregation rather than with liquation or re-solidification processes.

As mentioned in the experimental results, γ' precipitation differs between 600°C and 900°C. These differences were assessed by thermodynamic analysis, in which the phase-field method (PFM) coupled with the CALPHAD database is utilized [27]. The PFM is applied to γ' precipitation and growth in the γ matrix. Firstly, the solidified cellular microstructure evolution during the rapid solidification of powder bed fusion, in which the typical cooling rate and temperature gradient were set 5×10^5 K/s and 5×10^6 K/m, respectively, was obtained as shown in Fig. 17 (a). This result is a part of a previous paper [27], in which CALPHAD and diffusion database, Thermo-Calc TCNI9 and MOBNI5 (https://thermocalc.com/products/databases/nickel-based-alloys/), were adapted, respectively. Other computational and physical conditions, such as grid size, boundary conditions, time step, initial γ grain size, interface energies and interface mobilities, are given in Ref. [27]. In this calculation, initial conditions consisted of a solid γ layer (five grid widths in thickness) set at the bottom of the simulated region. The two-dimensional solidification microstructure evolution of the γ phase was performed using the composition shown in Table 1. The trace elements, B, Zr and O, were omitted in this simulation. It is well known that boron segregation has ability to affect grain boundary γ' precipitation in 738LC. [28]. In the present PFM simualtion, it was confirmed that B addition together with C led to numeric instability in the thermodynamics calculations of CALPHAD coupling with PFM. The reason is that trace elements, C and B, having high activity, cause large numerical errors with slight composition deviations when both elements are present. In order to obtain a stable condition, only C addition was selected in the present PFM simulation. The typical cellular structure corresponding to rapid solidification was obtained as shown in Fig. 17 (a). Inverse segregation of the solute Al appeared in the boundary between cells. Other solute elements were confirmed to be normally or inversely segregated within the cell boundaries.

Precipitation and growth of γ' were also simulated by the same method. Fig. 17 (b) shows a magnified region of γ' precipitation and growth, taken from a 1 μm × 1 μm square, shown in Fig. 17 (a). Grid width and interface thickness were set as 0.01 μm and five grids, respectively. The time difference was 1×10^{-8}s. Interface energy was assumed to be 0.02 J/m^2, which is the approximate average value of the γ'/γ interface [29]. Interfacial mobility was adjusted and set to 2.5×10^{-12} m^4/J/s. Both values were assumed to be isotopic in this simulation. TCNI9 and MOBNI5 were also adapted to CALPHAD and diffusion database coupling. The precipitation driving force of γ' (FCC_L12#2, ordered lattice) relative to the γ matrix (FCC_L12#1 disordered lattice) obeys the parallel rule for Gibbs' free energy depending on the local solute concentration estimated by the CALPHAD method. In this study, nucleation was examined at positions arranged on a uniform grid with 0.1 μm spacing in both the horizontal and vertical directions. Elastic energy caused by γ' precipitation is not considered to add to total free energy. In other words, γ' precipitation and growth were evaluated by only chemical thermodynamics estimation. Therefore, the phase-field calculations are intended to provide a qualitative comparison of the thermodynamic tendency for γ' formation at different temperatures, rather than to reproduce the temporal or mechanical history of the elevated-temperature tensile experiments. The nucleation model for γ' was implemented using a Poisson-seed approach, which captures stochastic nucleation events even with the relatively large time steps used in the PFM. For this work, we adopted the detailed numerical method proposed by M. Yang, L. Wang, and W. Yan [30].

In their Poisson-seed approach for PFM, the nucleation probability P_n is expressed as,

$$P_n = 1 - exp\left(-J \cdot \Delta t \cdot \Delta x^3\right), \tag{1}$$

where Δx and Δt are the grid width and time difference of PFM, respectively. J is the nucleation rate that is based on classical nucleation

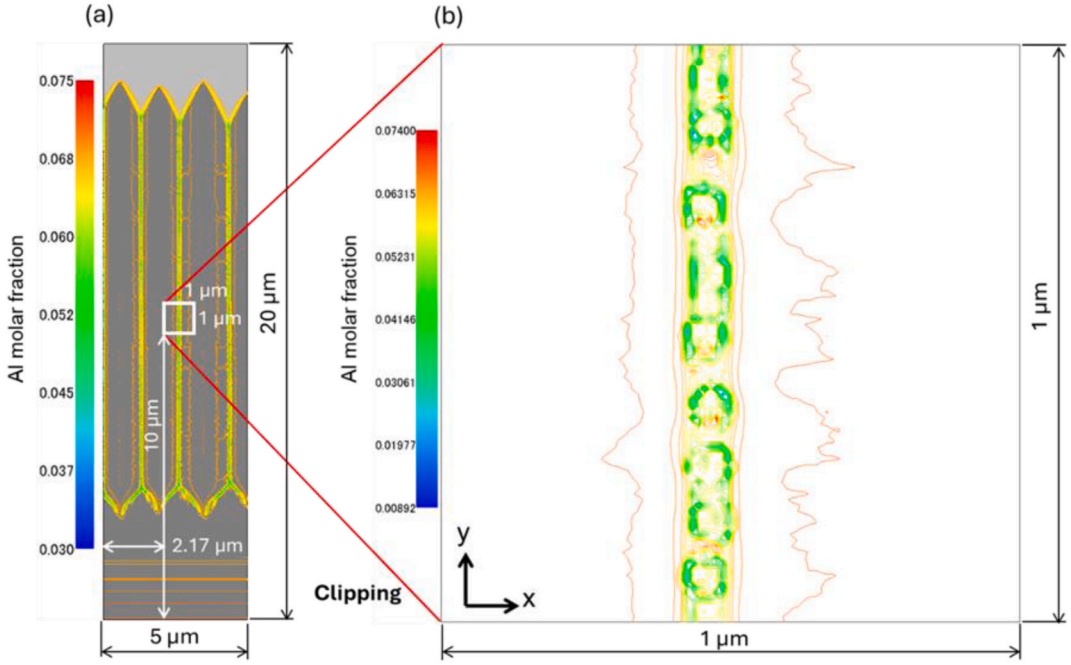


Fig. 17. Cellular microstructure evaluation of rapid solidification. (a) Al concentration distribution, (b) Magnified region of cell boundary showing initial condition for γ' precipitation.

theory. It is given as,

$$J = Z\frac{kTN_{atm}}{h}\cdot exp\left(-\frac{Q_D}{RT}\right)\cdot exp\left(-\frac{\Delta g_V \cdot f(\theta)}{kT}\right), \quad (2)$$

where Z is the Zeldovich number which is usually defined as $10^{-3} \sim 10^{-2}$. It was assumed to be 0.002. k and h are Boltzmann and Plank constants, respectively. N_{atm} is number of atoms in the γ/γ' interface region. It is estimated to be 9.139×10^{28} m^{-3} for pure Ni. Q_D is the activation energy for diffusion, 1.458×10^5 J/mol, which was obtained from the diffusion database MOBNI5 for IN738LC. $f(\theta)$ is the contact angle function of heterogeneous nucleation. In this simulation, γ' is assumed to form by homogeneous nucleation, $f(\theta) = 1$. Δg_V is the maximum free energy for nucleation and is expressed as,

$$\Delta g_V = \frac{16\pi}{3}\cdot\frac{{\sigma_p}^3}{(\Delta G_V)^2} \quad (3)$$

where σ_p is interfacial energy at the γ/γ' interface and is equal to 0.02 J/m^2 as explained previously. ΔG_V is the driving force of γ' formation within the γ phase, which was directly estimated by CALPHAD database coupling in the PFM calculation. This thermodynamical estimation was performed at each grid point and every time step in the PFM CALPHAD coupling procedure.

Before PFM calculation, the nucleation probability (Pn) distribution as a function of temperature was confirmed using simplified driving force ΔG_V, which is approximated as,

$$\Delta G_V = L_m\cdot\frac{\Delta T}{T_\gamma} \quad (4)$$

From CALPHAD database, the transformation temperature T_γ and the latent heat L_m for IN738LC were 1395K and 1.257×10^4 J/ mol, respectively. Fig. 18 shows the nucleation probability P_n with temperature.

It is understood that nucleation probability is approximately zero at 600°C and sharply increases around 800°C. PFM Simulations were performed at 600°C and 900°C. Nucleation of γ' did not occur at 600°C as predicted by an almost zero nucleation probability in Fig. 18. This result further suggests that γ' forms by spinodal decomposition rather than by precipitation.

On the other hand, at 900°C, γ' precipitation and growth was confirmed as shown in Fig. 19 (a), in which the holding time was 0.15 ms. The γ' nucleates and grows in a way that is qualitatively the same as that observed in the experiments. It is also confirmed that the γ' forming elements, Ti and Al, are present in high concentrations in the precipitated grains, as shown in Fig. 19(b) and (c), respectively. The segregation behavior shown in Fig. 19 is considered qualitatively equivalent to that observed along the grain boundary in Fig. 13. Therefore, it is expected that a layer of γ' will form via nucleation and growth along the grain boundaries at temperatures above 800°C, as observed in the experiments.

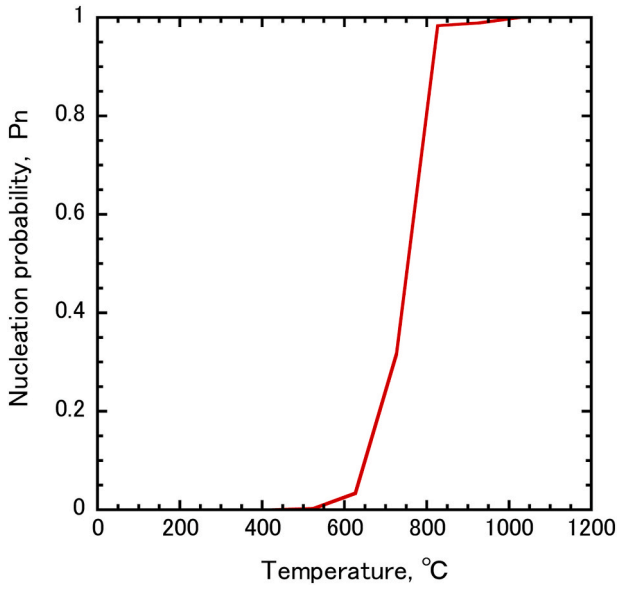


Fig. 18. Nucleation probability of γ' with temperature from classical nucleation modeling coupled with the CALPHAD database.

The weakening of the grain boundaries by the intermetallic γ' phase is believed to be a major contributory factor in the observed DDC phenomenon. The generally accepted explanation of DDC is that grain hardening by γ' precipitation within the grain causes stress relaxation via grain boundary sliding during plastic deformation, and grain boundary cracking (DDC) occurs where grain boundary sliding is sufficiently concentrated (very often at triple points) [11]. EBSD-KAM maps reveal localized regions of elevated kernel average misorientation adjacent to crack tips. These regions indicate localized plastic deformation associated with crack propagation. While KAM does not directly demonstrate grain-boundary sliding, the observations are consistent with localized plastic strain occurring during ductility-dip cracking. The present results therefore suggest that the formation of thin grain-boundary layer of γ' may weaken the grain boundaries, thereby exacerbating this type of cracking. Grain boundary γ' has been observed by Ramakrishnan and Dinda [9] to be the cause of liquation cracking in Inconel 738 fabricated by laser metal deposition (LMD). However, the grain boundary γ' in that work was in the form of larger particles, up to 700 nm in diameter, arranged in bands along the boundaries. Chen et al. [31] reported that extensive grain boundary γ' precipitation in the Ni-based superalloy Udimet 720Li, particularly as a γ/γ' cellular structure, can cause a loss of grain boundary cohesion, leading to a shorter creep life. The presence of grain boundary γ' can lead to strengthening in Ni-based superalloys but at the cost of a loss of ductility, and the current study has shown that a thin discontinuous layer of γ', only about 40 nm in thickness, may significantly contribute to the extensive intra-columnar grain boundary cracking and associated ductility reduction observed during tensile loading of additively manufactured Inconel 738LC at 900°C.

The presence of boron at the high angle grain boundaries following testing at both 600°C and 900°C is also noteworthy. Theska et al. [32] report that segregation of B and Zr promote both M_2B and γ' precipitation at grain boundaries in René 41, which in turn reduce grain boundary cohesion and promote cracking. Therefore, it is entirely possible that the segregation of boron to grain boundaries observed in this study, played a role in the precipitation of the γ', and the possible reduction in grain-boundary cohesion.

It should be noted that although the present observations provide strong evidence for an association between grain-boundary γ′ precipitation, elemental segregation, and intergranular cracking, they do not directly quantify grain-boundary cohesion or directly demonstrate grain-boundary sliding. Furthermore, the microstructural characterization was concentrated on the temperatures exhibiting the greatest contrast in cracking behavior and does not fully resolve the evolution of grain-boundary precipitation and segregation across the entire ductility-dip temperature range.

Future work combining high-resolution microscopy with in-situ mechanical testing or direct measurements of grain-boundary strength would provide further insight into the relationship between grain boundary γ′ precipitation, boundary cohesion, and ductility-dip cracking.

5. Conclusions

The cracking behavior of Inconel 738LC fabricated via L-PBF during elevated temperature tensile deformation was investigated. The

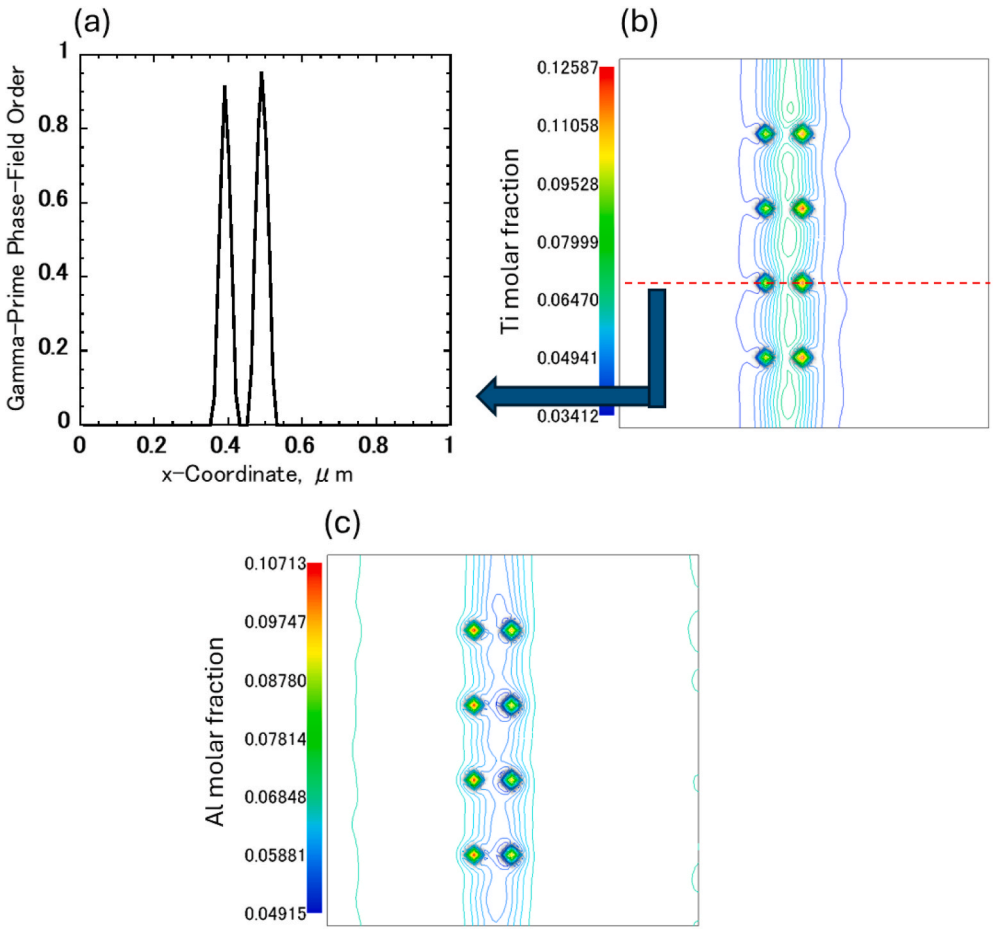


Fig. 19. γ' and solute concentration distributions at holding time 0.15 ms at 900°C. (a) γ' PFM order distribution on the cross-section at the y-coordinate, 0.4 μm, (b), (c) Ti and Al molar fractions.

following conclusions can be drawn.

1. Ductility-dip cracking occurs under tensile loading in the as-fabricated Inconel 738LC at temperatures around 800°C – 900°C. The cracks are located at high angle grain boundaries within the vertical columnar grains of the as-fabricated microstructure.
2. The DDC appears in combination with significant γ' precipitation both within the metal matrix and along grain boundaries.
3. Strong segregation of boron to grain boundaries was identified in this additively manufactured Inconel 738LC alloy following tensile loading at temperatures from 600°C to 900°C. Strongest boron segregation occurred in regions where the γ phase was present on either side of the grain boundary, consistent with its role in stabilizing and strengthening γ/γ boundaries.
4. The prevalence of ductility-dip cracking at temperatures of 800-900°C in this material is explained by the precipitation of a 40 nm thick discontinuous layer of the intermetallic γ' phase along grain boundaries in this temperature range. Theoretical modeling using the phase-field method has determined that γ' will form exclusively via nucleation and growth at temperatures above 800°C, and via spinodal decomposition below 600°C. The results suggest that presence of a thin grain-boundary layer of γ' may be associated with reduced grain-boundary cohesion, thereby facilitating grain-boundary sliding and contributing to intergranular cracking. The segregation of boron may also play a role in the formation of the grain boundary γ'.
5. Further optimization of AM processing parameters is required to suppress element segregation, and hence, reduce the propensity for subsequent grain boundary γ' formation. Preheating of the substrate during L-BPF processing, or the use of electron beam melting AM methods which permit high build-chamber temperatures and lower cooling rates, are possible ways to achieve this goal.

CRediT authorship contribution statement

Christopher Mercer: Writing – review & editing, Writing – original draft, Investigation. **Taisuke T. Sasaki:** Writing – review & editing, Writing – original draft, Investigation. **Yuka Hara:** Investigation. **Toru Hara:** Writing – review & editing, Supervision. **Masahiro Kusano:** Investigation. **Sukeharu Nomoto:** Formal analysis. **Makoto Watanabe:** Writing – review & editing, Supervision, Conceptualization.

Ethical approval

Not Applicable.

Declaration of competing interest

The authors declare that they have no known competing financial interests or personal relationships that could have appeared to influence the work reported in this paper.

Acknowledgments

This work was partly supported by K-Program Grant Number JPMJKP25R1 (Funding agency: JST), and by a grant from the Amada Foundation (No. AF-2022201-A3) and a JSPS KAKENHI Grant-in-Aid for Transformative Research Areas (A) "Creation of Materials by Super

Thermal Field: Neo-3D printing by Manipulating Atomic Arrangement through Giant Potential Gradient" (Grant Number 24H01008). In addition, the authors are very grateful to Mr. Tomoki Tashiro, Ms. Rie Matsumoto, Ms. Ayako Hosokai and Dr. Alok Singh at the National Institute for Materials Science for their technical support.

Data availability

The data that has been used is confidential.

References

[1] C. Hays, Size and shape effects for gamma prime in alloy 738, J Mater Eng & Performance 17 (2008) 254–259, https://doi.org/10.1007/s11665-007-9135-y.
[2] O.A. Ojo, N.L. Richards, M.C. Chaturvedi, Study of the fusion zone and heat-affected zone microstructures in tungsten inert gas-welded INCONEL 738LC superalloy, Metall. Mater. Trans A 37A (2006) 421–433, https://doi.org/10.1007/s11661-006-0013-2.
[3] A.T. Egbewande, H.R. Zhang, R.K. Sidhu, O.A. Ojo, Improvement in laser weldability of INCONEL 738 superalloy through microstructural modification, Metall. Mater. Trans A 40A (2009) 2694–2704, https://doi.org/10.1007/s11661-009-9962-6.
[4] J.C. Lippold, S.D. Kiser, J.N. DuPont, Welding Metallurgy and Weldability of Nickel-Base Alloys, John Wiley & Sons, 2011.
[5] M. Cloots, P.J. Uggowitzer, K. Wegener, Investigations on the microstructure and crack formation of IN738LC samples processed by selective laser melting using gaussian and doughnut profiles, Mater. Des. 89 (2016) 770–784, https://doi.org/10.1016/j.matdes.2015.10.027.
[6] J. Xu, X. Lin, Y. Zhao, P. Guo, X. Wen, Q. Li, H. Yang, H. Dong, L. Xue, W. Huang, HAZ liquation cracking mechanism of IN-738LC superalloy prepared by laser solid forming, Metall. Mater. Trans. A 49A (2018) 5118–5136, https://doi.org/10.1007/s11661-018-4826-6.
[7] H. Gruber, E. Hryha, K. Lindgren, Y. Cao, M. Rashidi, L. Nyborg, The effect of boron and zirconium on the microcracking susceptibility of IN-738LC derivatives in laser powder bed fusion, Appl. Surf. Sci. 573 (2022) 151541, https://doi.org/10.1016/j.apsusc.2021.151541.
[8] A. Després, S. Antonov, C. Mayer, C. Tassin, M. Veron, J.-J. Blandin, P. Kontis, G. Martin, On the role of boron, carbon and zirconium on hot cracking and creep resistance of an additively manufactured polycrystalline superalloy, Materialia 19 (2021) 101193, https://doi.org/10.1016/j.mtla.2021.101193.
[9] A. Ramakrishnan, G.P. Dinda, Direct laser metal deposition of inconel 738, Mater. Sci. Eng., A 740–741 (2019) 1–13, https://doi.org/10.1016/j.msea.2018.10.020.
[10] L. Rickenbacher, T. Etter, S. Hövel, K. Wegener, High temperature material properties of IN738LC processed by selective laser melting (SLM) technology, Rapid Prototyp. J. 19 (2013) 282–290, https://doi.org/10.1108/13552541311323281.
[11] X. Zhang, H. Chen, L. Xu, J. Xu, X. Ren, X. Chen, Cracking mechanism and susceptibility of laser melting deposited Inconel 738 superalloy, Mater. Des. 183 (2019) 108105, https://doi.org/10.1016/j.matdes.2019.108105.
[12] M. Caruso, L. Frame, Ductility dip cracking mechanisms and characterization: a review, J. Mater. Sci. 59 (2024) 16789–16814, https://doi.org/10.1007/s10853-024-10112-w.
[13] L. Zheng, G. Schmitz, Y. Meng, et al., Mechanism of intermediate temperature embrittlement of Ni and Ni-based superalloys, Crit. Rev. Solid State Mater. Sci. 37 (2022) 181–214, https://doi.org/10.1080/10408436.2011.613492.
[14] F.N. Rhines, P.J. Wray, Investigation of the intermediate temperature ductility minimum in metals, ASM Trans Q 54 (1961) 117–128.
[15] A.J. Ramirez, J.C. Lippold, High temperature behavior of Ni-base weld metal Part I. Ductility and microstructural characterization, Mater. Sci. Eng., A 380 (2004) 259–271, https://doi.org/10.1016/j.msea.2004.03.074.
[16] A.J. Ramirez, J.C. Lippold, High temperature behavior of Ni-base weld metal Part II—Insight into the mechanism for ductility dip cracking, Mater. Sci. Eng., A 380 (2004) 245–258, https://doi.org/10.1016/j.msea.2004.03.075.
[17] C. Fink, An investigation on ductility-dip cracking in the base metal heat-affected zone of wrought nickel base alloys— part I: metallurgical effects and cracking mechanism, Weld. World 60 (2016) 939–950, https://doi.org/10.1007/s40194-016-0370-4.
[18] A. Eilers, J. Nellesen, R. Zielke, W. Tillmann, Analysis of the ductility dip cracking in the nickel-base alloy 617mod, in: 19th Chemnitz Seminar on Materials Engineering, Institute of Physics Publishing, 2017 012020, https://doi.org/10.1088/1757-899X/181/1/012020.
[19] W. Mo, S. Lu, D. Li, Y. Li, Effects of $M_{23}C_6$ on the high-temperature performance of Ni-based welding material NiCrFe-7, Metall. Mater. Trans. A 45A (2014) 5114–5126, https://doi.org/10.1007/s11661-014-2439-2.
[20] W. Mo, X. Hu, S. Lu, et al., Effects of boron on the microstructure, ductility-dip-cracking, and tensile properties for NiCrFe-7 weld metal, J. Mater. Sci. Technol. 31 (2015) 1258–1267, https://doi.org/10.1016/j.jmst.2015.08.001.
[21] M.J. Cola, D.F. Teter, Optical and analytical electron microscopy of ductility-dip cracking in Ni-Base filler metal 52—Initial Studies, in: 5th International Conference on Trends in Welding Research, Pine Mountain, 1998, https://doi.org/10.2172/319823.
[22] M. Perrot-Simonetta, A. Koblyanski, Influence of trace elements on hot ductility of an ultra high purity invar alloy, J. Phys. IV - Proc. 5 (1995) 323–334, https://doi.org/10.1051/jp4:1995739.
[23] K. Nishimoto, K. Saida, H. Okauchi, Microcracking in multipass weld metal of alloy 690 part 1—Microcracking susceptibility in reheated weld metal, Sci. Technol. Weld. Join. 11 (2006) 455–461, https://doi.org/10.1179/174329306X94291.
[24] K. Nishimoto, K. Saida, H. Okauchi H, K. Ohta, Microcracking in multipass weld metal of alloy 690 Part 2—Microcracking mechanism in reheated weld metal, Sci. Technol. Weld. Join. 11 (2006) 462–470, https://doi.org/10.1179/174329306X94309.
[25] THE INTERNATIONAL NICKEL COMPANY, INC., Alloy IN738 Technical Data.
[26] D.M. Collins, N. D'Souza, C. Panwisawas, et al., Spinodal decomposition versus classical γ′nucleation in a nickel-base superalloy powder: an in-situ neutron diffraction and atomic-scale analysis, Acta Mater. 200 (2020) 959–970, https://doi.org/10.1016/j.actamat.2020.09.055.
[27] S. Nomoto, M. Kusano, H. Kitano, M. Watanabe, Multi-Phase field method for solidification microstructure evolution for a Ni-Based alloy in wire arc additive manufacturing, Metals 12 (2022) 1720, https://doi.org/10.3390/met12101720.
[28] C. Guo, G. Li, F. Zhou, et al., Understanding the significant effect of boron content on the printability of IN738LC superalloy fabricated using laser powder bed fusion, Opt Laser. Technol. 159 (2023) 108954, https://doi.org/10.1016/j.optlastec.2022.108954.
[29] S.X. Liang, K.Y. Liu, Y.X. Zhou, et al., Interfacial energy between γ/γ' phases of Ni–Al alloys extracted by using a new method, Mater. Chem. Phys. 277 (2022) 125538, https://doi.org/10.1016/j.matchemphys.2021.125538.
[30] M. Yang, L. Wang, W. Yan, Phase-field modeling of grain evolutions in additive manufacturing from nucleation, growth, to coarsening, Computational Materials 7 (2021) 56, https://doi.org/10.1038/s41524-021-00524-6.
[31] T.-W. Chen, B.-C. Wu, Y.-C. Kang, et al., The impact of grain boundary serration treatments on the creep deformation of Udimet-720Li superalloy, Mater. Sci. Eng., A 924 (2025) 147729, https://doi.org/10.1016/j.msea.2024.147729.
[32] F. Theska, R. Buerstmayr, H. Liu, et al., Influence of grain boundary precipitation and segregation on cracking of cast and wrought superalloys containing B and Zr, Mater. Charact. 187 (2022) 111881, https://doi.org/10.1016/j.matchar.2022.111881.